Lawrence Berkeley National Laboratory

Title
IPTF16fnl: A Faint and Fast Tidal Disruption Event in an E+A Galaxy

Permalink
https://escholarship.org/uc/item/5bs5q12r

Journal
Astrophysical Journal, 844(1)

ISSN
0004-637X

Authors
Blagorodnova, N
Gezari, S
Hung, T
et al.

Publication Date
2017-07-20

DOI
10.3847/1538-4357/aa7579

Peer reviewed

iPTF16fnl: A FAINT AND FAST TIDAL DISRUPTION EVENT IN AN E+A GALAXY

N. Blagorodnova [1], S. Gezari [2,3], T. Hung [2], S. R. Kulkarni [1], S. B. Cenko [3,4], D. R. Pasham [5,26†], L. Yan [1,6],
I. Arcavi [7,8,26†], S. Ben-Ami [9,10], B. D. Bue [11], T. Cantwell [12], Y. Cao [13], A. J. Castro-Tirado [14,15], R. Fender [16],
C. Fremling [17], A. Gal-Yam [10], A. Y. Q. Ho [1], A. Horesh [18], G. Hosseinzadeh [7,8], M. M. Kasliwal [1],
A. K. H. Kong [16,19], R. R. Laher [6], G. Leloudas [10,20], R. Lunnan [1,17], F. J. Masci [6], K. Mooley [16], J. D. Neill [1],
P. Nugent [21,22], M. Powell [23], A. F. Valeev [24], P. M. Vreeswijk [10], R. Walters [1], P. Wozniak [25]
(Dated: Received XX XX XXXXX; accepted XX XX, XXXX)

[1] Cahill Center for Astrophysics, California Institute of Technology, Pasadena, CA 91125, USA; nblago@caltech.edu

[2] Department of Astronomy, University of Maryland, Stadium Drive, College Park, MD 20742-2421, USA

[3] Joint Space-Science Institute, University of Maryland, College Park, MD 20742, USA

[4] NASA Goddard Space Flight Center, Mail Code 661, Greenbelt, MD 20771, USA

[5] Center for Space Research, Massachusetts Institute of Technology, Cambridge, MA 02139

[6] Infrared Processing and Analysis Center, California Institute of Technology, Pasadena, CA 91125, USA

[7] Department of Physics, University of California, Santa Barbara, CA 93106-9530, USA

[8] Las Cumbres Observatory, 6740 Cortona Dr Ste 102, Goleta, CA 93117-5575, USA

[9] Smithsonian Astrophysical Observatory, Harvard-Smithsonian Center for Astrophysics, 60 Garden St., Cambridge, MA 02138, USA

[10] Department of Particle Physics and Astrophysics, Weizmann Institute of Science, Rehovot 7610001, Israel

[11] Jet Propulsion Laboratory, California Institute of Technology, Pasadena, CA 91125, USA

[12] Jodrell Bank Centre for Astrophysics, Alan Turing Building, Oxford Road, Manchester M13 9PL, UK

[13] Department of Astronomy, University of Washington, Box 351580, Seattle, WA 98195-1580, USA

[14] Instituto de Astrofísica de Andalucía (IAA-CSIC), P.O. Box 03004, E-18080 Granada, Spain

[15] Unidad Asociada Departamento de Ingeniera de Sistemas y Automtica, Univ. de Málaga, Spain

[16] Astrophysics, Department of Physics, University of Oxford, Keble Road, Oxford OX1 3RH, UK

[17] Department of Astronomy, The Oskar Klein Center, Stockholm University, AlbaNova, 10691 Stockholm, Sweden

[18] Racah Institute of Physics, Hebrew University, Jerusalem, 91904, Israel

[19] Institute of Astronomy and Department of Physics, National Tsing Hua University, Hsinchu 30013, Taiwan

[20] Dark Cosmology centre, Niels Bohr Institute, University of Copenhagen, Juliane Maries vej 30, 2100 Copenhagen, Denmark

[21] Lawrence Berkeley National Laboratory, Berkeley, California 94720, USA

[22] Department of Astronomy, University of California, Berkeley, CA 94720-3411, USA

[23] Department of Physics and Yale Center for Astronomy & Astrophysics, Yale University PO Box 208120, New Haven, CT 06520-8120, USA

[24] Special Astrophysical Observatory, Nizhnij Arkhyz, Karachai-Cherkessian Republic, 369167 Russia

[25] Los Alamos National Laboratory, MS-D466, Los Alamos, NM 87545, USA

[26†] Einstein Fellow

ABSTRACT

We present ground-based and *Swift* observations of iPTF16fnl, a likely tidal disruption event (TDE) discovered by the intermediate Palomar Transient Factory (iPTF) survey at 66.6 Mpc. The lightcurve of the object peaked at absolute $M_g = -17.2$ mag. The maximum bolometric luminosity (from optical and UV) was $L_p \simeq (1.0 \pm 0.15) \times 10^{43}$ erg s^{-1}, an order of magnitude fainter than any other optical TDE discovered so far. The luminosity in the first 60 days is consistent with an exponential decay, with $L \propto e^{-(t-t_0)/\tau}$, where $t_0 = 57631.0$ (MJD) and $\tau \simeq 15$ days. The X-ray shows a marginal detection at $L_X = 2.4^{1.9}_{-1.1} \times 10^{39}$ erg s^{-1} (*Swift* X-ray Telescope). No radio counterpart was detected down to 3σ, providing upper limits for monochromatic radio luminosity of $\nu L_\nu < 2.3 \times 10^{36}$ erg s^{-1} and $\nu L_\nu < 1.7 \times 10^{37}$ erg s^{-1} (VLA, 6.1 and 22 GHz). The blackbody temperature, obtained from combined *Swift* UV and optical photometry, shows a constant value of 19,000 K. The transient spectrum at peak is characterized by broad He II and Hα emission lines, with an FWHM of about 14,000 km s^{-1} and 10,000 km s^{-1} respectively. He I lines are also detected at $\lambda\lambda$ 5875 and 6678. The spectrum of the host is dominated by strong Balmer absorption lines, which are consistent with a post-starburst (E+A) galaxy with an age of ∼650 Myr and solar metallicity. The characteristics of iPTF16fnl make it an

outlier on both luminosity and decay timescales, as compared to other optically selected TDEs. The discovery of such a faint optical event suggests a higher rate of tidal disruptions, as low luminosity events may have gone unnoticed in previous searches.

Keywords: accretion, accretion discs – black hole physics – stars: individual (iPTF16fnl), galaxies: nuclei

1. INTRODUCTION

A tidal disruption event (TDE) is the phenomenon observed when a star is torn apart by the tidal forces of a supermassive black hole (SMBH), usually lurking in the core of its galaxy. As a consequence, a bright flare is expected when some of the bound material accretes onto the SMBH. Although such events were theoretically predicted a few decades ago (Hills 1975; Lacy et al. 1982; Rees 1988; Evans & Kochanek 1989; Phinney 1989), observational signatures are more recent. The first detection of TDEs were made in the soft X-ray data. The flares, consistent with the proposed stellar disruption scenario, were identified in ROentgen SATellite (ROSAT) all-sky survey (Bade et al. 1996; Komossa & Bade 1999; Saxton et al. 2012). Detection in gamma-ray data of *Swift* events Swift J1644+75 (Bloom et al. 2011; Levan et al. 2011; Burrows et al. 2011; Zauderer et al. 2011; Cenko et al. 2012) and Swift J1112.2-8238 (Brown et al. 2015) were attributed to relativistic outbursts caused by jetted emission. We refer the reader to Komossa (2015); Auchettl et al. (2016) for a broader review of the status of observations in different wavelengths.

Ultraviolet detections of nuclear flares were reported from the *GALEX* survey (Gezari et al. 2006, 2008, 2009). TDEs are now being discovered by optical surveys such as the Sloan Digital Sky Survey (SDSS; van Velzen et al. 2011), PanSTARRS-1 (PS1; Gezari et al. 2012; Chornock et al. 2014), Palomar Transient Factory (PTF; Arcavi et al. 2014), All Sky Automated Survey for Supernovae (ASAS-SN; Holoien et al. 2014, 2016b,a), Robotic Optical Transient Search Experiment (ROTSE Vinkó et al. 2015), Optical Gravitational Lensing Experiment (OGLE; Wyrzykowski et al. 2017) and the intermediate Palomar Transient Factory (iPTF; Hung et al. (2017), Duggan G. et. al. in prep and the work presented here). The optical sample has revealed that an important fraction of the TDEs appear to be found in E+A ("quiescent Balmer-strong") galaxies (Arcavi et al. 2014; French et al. 2016), which can be interpreted as middle-aged ($< 1\,\mathrm{Gyr}$) post-starburst galaxies (Zabludoff et al. 1996; Dressler et al. 1999).

Here we present iPTF16fnl, an optical TDE candidate discovered by iPTF. The event is localized in the center of an E+A galaxy. With a distance of 66.6 Mpc this is the closest well-studied event in optical/UV wavelengths.
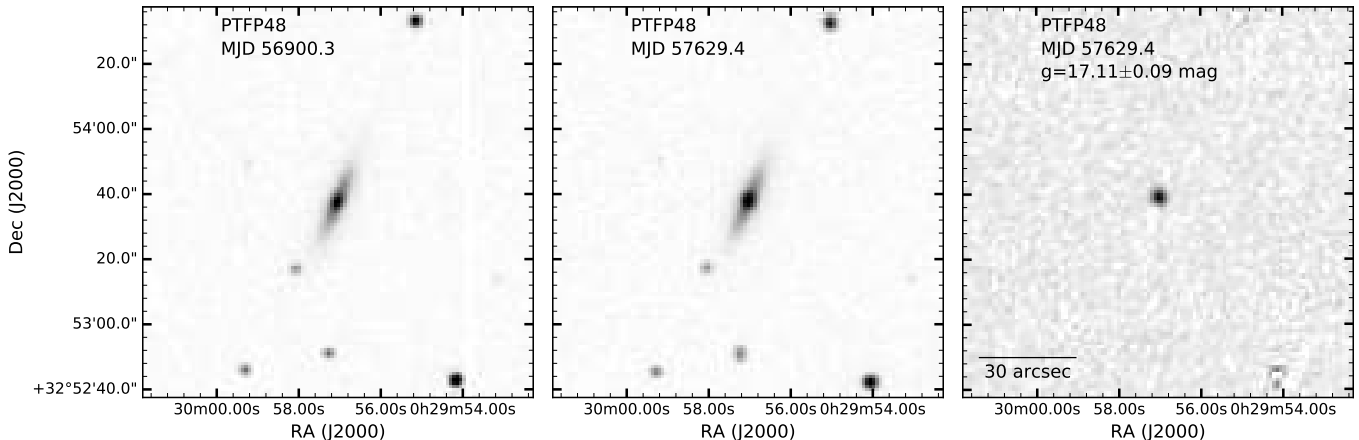
2. DISCOVERY AND HOST GALAXY

2.1. *Discovery and classification*

iPTF16fnl was discovered on UT 2016 August 29.4 in an image obtained during the g+R experiment (Miller et al. 2017): during the night, one image each was obtained in g and R band; the images are separated by at least an hour in order to filter out asteroids. The event was identified by two real-time difference imaging pipelines (Cao et al. 2016; Masci et al. 2017), shown in Figure 1. The discovery magnitudes were $g = 17.11 \pm 0.09$ and $R = 17.39 \pm 0.09$ (see Ofek et al. (2012) for photometric calibration of PTF). Given an RMS of $0.5''$, the coordinates of the source, $\alpha_{J2000} = 00^{\mathrm{h}}29^{\mathrm{m}}57^{\mathrm{s}}.04\ \delta_{J2000} = +32^{\mathrm{h}}53^{\mathrm{m}}37^{\mathrm{s}}.5$ (ICRS) are consistent with central position of the galaxy, as provided by the Sloan Digital Sky Survey (SDSS) catalogue (Alam et al. 2015).

The brightness, blue colour ($g - R = -0.28\,\mathrm{mag}$) and central location of the transient in its host galaxy, made it a prime candidate for prompt follow-up observation. On the night after discovery, we observed the source with the FLOYDS spectrograph (Sand et al. 2011) on the Las Cumbres Observatory (LCO; Brown et al. 2013) 2-m telescope and the Spectral Energy Distribution Machine (SEDM) on the Palomar 60-inch (P60) telescope. FLOYDS are a pair of robotic low-resolution ($R \sim 450$) slit spectrographs optimized for supernova classification and follow-up. The SEDM is a ultra-low resolution ($R \sim 100$) integral-field-unit (IFU) spectrograph, dedicated to fast turnaround classification (Blagorodnova N. et. al. in prep). The IFU's wide field-of-view of $28''$, allows for robotic spectroscopy. Their data reduction pipeline allow rapid reduction with minimal intervention from the user (aperture placing). Figure 2 shows the classification spectra, displaying a blue continuum and broad He II and Hα emission lines, characteristic of previously observed optical TDE spectra (Arcavi et al. 2014). The fast spectral identification of iPTF16fnl as a TDE candidate allowed us to rapidly inform the astronomical community (ATel #9433; Gezari et al. 2016), which in turn enabled numerous multi-wavelength follow-up campaigns.

2.2. *Host galaxy*

The host galaxy of iPTF16fnl is Markarian 950 (Mrk 950) located at z=0.016328 (Cabanela & Aldering 1998; Petrosian et al. 2007). Given the edge-on host in-

Figure 1. P48 cutouts of $2'$ diameter sky region centered in the position of the transient. The coordinates of the transient are $\alpha_{J2000} = 00^{\mathrm{h}}29^{\mathrm{m}}57^{\mathrm{s}}.05$, $\delta_{J2000} = +32^{\mathrm{h}}53^{\mathrm{m}}37^{\mathrm{s}}.48$. The cutouts show the host galaxy approximately one year before the discovery, on the day of the discovery, and the difference image showing the transient location in the core of the galaxy.
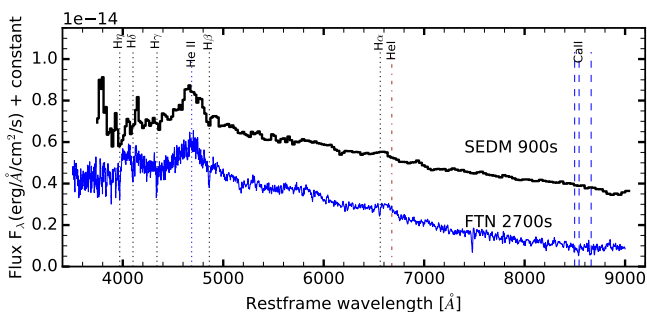
Figure 2. Two classification spectra obtained 2 days before the peak in g-band. The top black thick line shows the 900 s exposure obtained with SEDM, on the Palomar 60-inch (1.5 m). The bottom blue line shows a 2700 s exposure obtained with the FLOYDS spectrograph on the Las Cumbres Observatory (LCO) 2-m telescope. The blue continuum and prominent He II line are clearly identified in both spectra.

clination and the existence of a peculiar bar and nucleus, the galaxy is classified as Sp (*spindle*). The luminosity distance is $D_L = 66.6$ Mpc (distance modulus $\mu = 34.12$ mag) using $H_0 = 69.6\,\mathrm{km\,s^{-1}\,Mpc^{-1}}$, $\Omega_M = 0.29$, $\Omega_\Lambda = 0.71$ in the reference frame of the 3 K cosmic microwave background (CMB; Fixsen et al. 1996).

The estimated Galactic colour excess at the position of the transient is $E(B-V) = 0.062 \pm 0.001$ mag (from NED[1]), after adopting the extinction law of Fitzpatrick (1999) with corrections from Schlafly & Finkbeiner (2011). Assuming $R_V = 3.1$, the Galactic visual extinction is $A_V = 0.192$ mag.

The archival host magnitudes are shown in Table 1. The derived K-band luminosity of the galaxy is

Table 1. Archival photometry of Mrk 950.

Survey	Band	Magnitude (mag)	Reference
GALEX	FUV_{AB}	21.22 ± 0.39 [a]	[1]
GALEX	NUV_{AB}	20.191 ± 0.13 [a]	[1]
SDSSDR12	u	17.005 ± 0.012 [b]	[2]
SDSSDR12	g	15.491 ± 0.003 [b]	[2]
SDSSDR12	r	14.913 ± 0.003 [b]	[2]
SDSSDR12	i	14.585 ± 0.003 [b]	[2]
2MASS	J	13.212 ± 0.040	[3]
2MASS	H	12.545 ± 0.052	[3]
2MASS	K	12.360 ± 0.069	[3]
WISE	W1	13.075 ± 0.029	[4]
WISE	W2	13.086 ± 0.034	[4]
WISE	W3	12.331 ± 0.285	[4]
WISE	W4	>9.136	[4]
NVSS	1.4 GHz	<1.7 mJy	[5]
ROSAT	0.1-2.4 keV	$<1.04 \times 10^{-12}\ \mathrm{erg\,s^{-1}}$	[6]

[a] Measured within $7.5''$ diameter aperture. [b] Model magnitude. References: [1] Bianchi et al. (2011), [2] Alam et al. (2015), [3] Jarrett et al. (2000), [4] Wright et al. (2010), [5] Condon et al. (1998), [6] Voges et al. (1999)

$L_K = 1.15 \times 10^{10} \mathrm{L}_\odot$. Using the galaxy color $u - g = 1.5$, we compute a mass to light ratio for the K-band, $\log_{10}(M/L) = -0.0755$ (Bell et al. 2003), corresponding to a stellar mass $M_* \simeq 9.7 \times 10^9 \mathrm{M}_\odot$. Provided that size of the PSF in SDSS DR13 is an upper limit for the angular size of an unresolved bulge, we assume that an upper limit for the bulge-to-total ratio (B/T) can be estimated with an average (across all bands) value of `psfFlux`/`cModelFlux`$\sim 0.19 \pm 0.05$. We use this ratio to scale the total galaxy mass and derive $M_{BH} \leq 10^{6.6 \pm (0.1 + 0.34)} \mathrm{M}_\odot$, according to the $M_{BH} - M_{\mathrm{bulge}}$ re-

[1] The NASA/IPAC Extragalactic Database (NED) is operated by the Jet Propulsion Laboratory, California Institute of Technology, under contract with the National Aeronautics and Space Administration.

lation (McConnell & Ma 2013), including the 1σ scatter of 0.34 dex.

The age and metallicity of the host galaxy were determined by fitting a grid of galaxy models from Bruzual & Charlot (2003), using stellar evolutionary models from (Chabrier 2003). The fit was done using the `pPXF` code (Cappellari 2016). The best model was in agreement with a single burst of star formation with an age of 650 ± 300 Myr and a metallicity of Z=0.18 (here, $Z = 0.2$ corresponds to that of the Sun).

We use the high resolution spectrum taken with VLT/UVES taken two weeks after discovery (see log in Table 1, PI: P. Vreeswijk) to measure the host velocity dispersion. We obtain $v_{\rm host} = 89\pm1\,{\rm km\,s^{-1}}$, from the Ca II $\lambda\lambda8544,8664$ absorption lines. According to the M$-\sigma$ relation (McConnell & Ma 2013), this corresponds to a $M_{BH} = 10^{6.33\pm0.38}\,{\rm M}_\odot$, consistent with our previous estimate.

The field of iPTF16fnl was extensively observed for the last six years by PTF/iPTF. No prior activity in the host is detected with upper limits of $\sim$20-21 mag. The most recent non-detection is from MJD 57432.6, around 194 days before discovery. The host galaxy was also monitored by The Catalina Real-Time Transient Survey (CRTS; Drake et al. 2009) during 2006-2016 period. The magnitude of the galaxy was stable within the errors, with an unfiltered average magnitude of 14.88 ± 0.05 mag.

3. FOLLOW-UP OBSERVATIONS

3.1. *Photometric observations*

Following spectroscopic identification of iPTF16fnl as a TDE candidate, the source was monitored at Palomar and the Ultraviolet and Optical Telescope (UVOT; Roming et al. 2005) on board the *Swift* observatory (Gehrels et al. 2004). The UVOT observations were taken in *UVW2*, *UVM2*, *UVW1*, *U*, *B* and *V*; see Table 2. The data were reduced using the software `UVOTSOURCE` using the calibrations described in Poole et al. (2008) and updated calibrations from Breeveld et al. (2010). We use a $7.5''$ aperture centered on the position of the transient.

At Palomar, photometry in the g and Mould-R bands were obtained with the iPTF mosaic wide-field camera on the Palomar 48-inch telescope (P48; Rahmer et al. 2008). Difference-image photometric measurements were provided by the IPAC Image Subtraction and Discovery Pipeline developed for the iPTF survey (PTFIDE; Masci et al. 2017). Difference-imaging photometry in the $u'g'r'i'$ bands, obtained with the SEDM, were computed using the `FPipe` software (Fremling et al. 2016). The zeropoints were calibrated using stars in the SDSS footprint. Table 2 reports the mea-

Table 2. 3σ upper limits on radio emission for iPTF16fnl.

| Date	Telescope	Frequency	Flux
(UT)		(GHz)	(Jy)
2016 Aug 31	VLA	6.1, 22	$< 12 \times 10^{-6}$
2016 Sep 01	AMI	15	$< 117 \times 10^{-6}$
2016 Sep 05	AMI	15	$< 117 \times 10^{-6}$
2016 Sep 09	JCMT/SCUBA2	352	$< 10 \times 10^{-3}$
2016 Sep 10	JCMT/SCUBA2	352	$< 7.5 \times 10^{-3}$
2016 Sep 17	AMI	15	$< 117 \times 10^{-6}$
2016 Oct 22	AMI	15	$< 75 \times 10^{-6}$

sured *Swift* aperture photometry magnitudes and the difference imaging photometry for the Palomar data.

The multi-band *Swift* and optical lightcurve, corrected for Galactic extinction, is shown in Figure 3. To correct the UV bands for host light contamination, we used the average of the last four epochs of *Swift* data, from MJD 57712.7 to 57724.7 (> 80 days), to subtract from the early part of the lightcurve. The measurements were constant with an RMS of $\sim$0.05 mag, comparable to the measurement error. Optical *Swift* data were excluded from the analysis, as they were dominated by the host, not by the central point source.

In order to estimate the extinction in the host galaxy, we use all available *Swift* UV data and difference imaging photometry in *ugri* bands to fit blackbody emission curves, as detailed in Section 4. For each epoch, the photometry is corrected for both Galactic (fixed) and additional host extinction $E(B-V)$ from 0 to 0.25 mag in 0.05 steps. The likelihood between the de-reddened photometry and a blackbody model is computed for each epoch. In a final step, we marginalize over all epochs to derive the final value. We find that the best fit corresponds to $E(B-V)$=0, with an upper limit of $E(B-V)$=0.05. The selection of different extinction laws for host extinction (Calzetti et al. 2000; Fitzpatrick 1999) does not change our conclusions. Given the assumption that the emission from iPTF16fnl in fact follows a distribution, from now on we will assume the reddening in the host to be negligible.

3.2. *Radio observations*

Radio follow-up observations of iPTF16fnl were taken with the Jansky Very Large Array (VLA; PI A. Horesh), the Arcminute Microkelvin Imager (AMI; PI K. Mooley) and the James Clerk Maxwell Telescope and the Submillimetre Common-User Bolometer Array 2 (JCMT/SCUBA-2; PI A. K. H. Kong). The upper limits corresponding to the observations are shown in Table 2. The limits for the monochromatic radio luminosities corresponding to the first VLA epoch are $\nu L_\nu < 2.3 \times 10^{36}$ erg s^{-1} and $\nu L_\nu < 1.7 \times 10^{37}$ erg s^{-1} at 6.1 and 22 GHz.
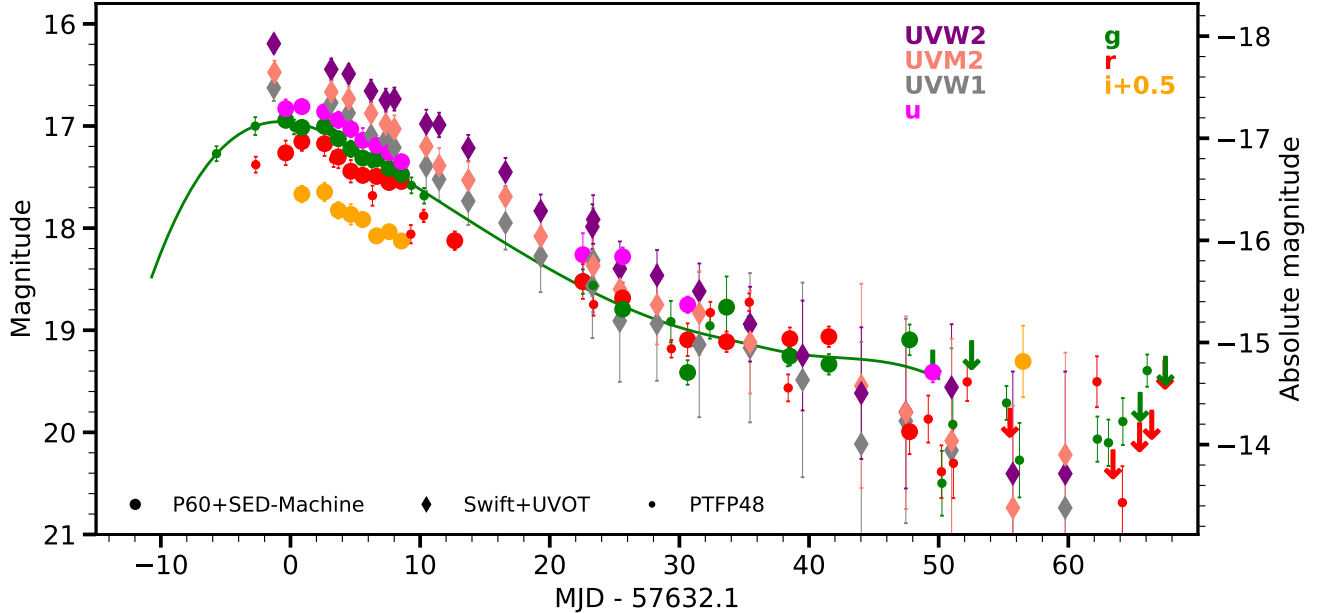
Figure 3. Observed lightcurve for iPTF16fnl. The green solid line shows the best fit spline to the g-band data, which was corrected for Galactic extinction. The errors for epochs later than 30 days are likely underestimated, as the bulge of the host is ~ 4 magnitudes brighter than the transient. The time of peak in g-band, MJD 57632.1 is used as the reference epoch. The small symbol "S" on top shows the epochs when spectra were taken. (A color version of this figure is available in the online journal.)

These limits are respectively two and one order of magnitude deeper than the VLA detection of ASASSN-14li at peak for a similar frequency range (van Velzen et al. 2016; Alexander et al. 2016).
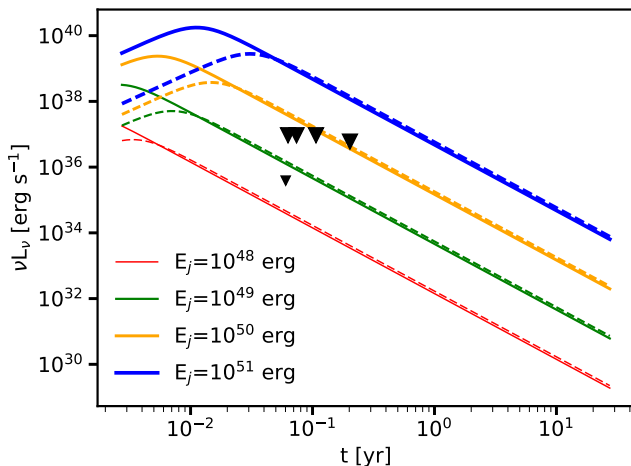
Figure 4. Upper limits for our 6 GHz (small triangle) and 15 GHz (big triangles) observations. The lines show analytic lightcurves for different TDE on-axis jet energies (colour coded) from Generozov et al. (2017). Solid lines represent the lightcurves for 15 GHz and dashed lines for 6 GHz. We assume $n_{18} = 11$ and the fiducial values provided in their models for an optically thick case. The results are also consistent with an optically thin case. The X-axis is computed relative to our lower limit of 11 days for the time to peak light.

We can use the limits reported here to argue against the presence of an on-axis relativistic outflow, or at least constrain the energy of the jet, E_j. We compare our limits in 6 and 15 GHz with the analytical lightcurves for on-axis TDE radio emission from Generozov et al. (2017). Figure 4 shows that our early time observations suggest jet energies with $E_j < 10^{49}\,\mathrm{erg\,s^{-1}}$.

Additionally, we contrast our measurements, scaled to the redshift of PS1-11af, with the GRB afterglow models of van Eerten et al. (2012) presented in Chornock et al. (2014) (their figure 13). Based on our non-detections, we can rule out the existence of a relativistic jet, as viewed $30°$ off-axis. For larger angles, the radio emission is expected to arise at later times (> 1 year after disruption). Therefore, continuous monitoring of the event at radio wavelengths is encouraged.

3.3. X-ray observations

We observed the location of iPTF16fnl with the X-Ray Telescope (XRT; Burrows et al. 2005) on-board the *Swift* satellite beginning at 19:32 UT on 30 August 2016. Regular monitoring of the field in photon counting (PC) mode continued over the course of the next four months (PIs T. Holoien and B. Cenko).

No significant emission is detected in individual epochs (typical exposure times of $\approx 2\,\mathrm{ks}$). Using standard XRT analysis procedures (e.g., Evans et al. 2009), we place 90% confidence upper limits ranging from (3.8–12.1) $\times 10^{-3}$ counts s^{-1} in the 0.3–10.0 keV bandpass

over this time period.

Stacking all the XRT data obtained over this period together (58 ks of total exposure time), we find evidence for a weak ($\approx 4\sigma$ significance) X-ray source at this location with a 0.3–10.0 keV count rate of $(2.6 \pm 1.2) \times 10^{-4}$ counts s^{-1}.

With only 15 source counts we have limited ability to discriminate between spectral models; however, with several photon energies detected above 1 keV. We derive response matrices for the stacked XRT observations using standard *Swift* tools. Adopting a power-law model for the spectrum with a photon index of 2 and accounting for line-of-sight absorption in the Milky Way (Willingale et al. 2013), we find the measured count rate corresponds to an unabsorbed flux of 0.3–10.0 keV flux of $4.6^{+3.7}_{-2.0} \times 10^{-15}$ erg cm^{-2} s^{-1}.

At the distance of Mrk 950, this corresponds to an X-ray luminosity of $L_X = 2.4^{+1.9}_{-1.1} \times 10^{39}$ erg s^{-1}. Without additional information (e.g., variability and/or spectra), we cannot determine conclusively if this X-ray emission is associated with the transient iPTF16fnl, or if this is unrelated X-ray emission from the host nucleus (e.g., an underlying active galactic nucleus) or even a population of X-ray binaries or ultra-luminous X-ray sources. However, the lack of evidence for ongoing star formation or AGN-like emission lines in the late-time optical spectra of Mrk 950 (§5) suggest an association with the tidal disruption event.

If this is indeed the case, the implied X-ray emission would be extremely faint, both in an absolute and a relative sense. We can contrast, for example, with the X-ray emission observed from ASASSN-14li (Holoien et al. 2016b; van Velzen et al. 2016), with a peak luminosity approximately four orders of magnitude above that seen for iPTF16fnl. Even sources with much fainter X-ray emission, such as ASASSN-15oi (Holoien et al. 2016a), still outshine iPTF16fnl by more than a factor of 100.

3.4. *Spectroscopic Observations*

Spectroscopic follow-up observations of iPTF16fnl have been carried out with numerous telescopes and instruments, summarized in the spectroscopic log in Table 1. Figure 5 shows the spectral sequence for iPTF16fnl, spanning three months. The spectroscopic data are made public via WISeREP (Yaron & Gal-Yam 2012).

Given the brightness of the galactic bulge relative to the TDE, the interpretation of the TDE spectrum poses some challenges. A noticeable feature is the strong host component in all the available spectra. Different slit widths, the variable seeing, different orientations of the slit during the acquisition of the data (generally taken at the parallactic angle) and the highly elongated geometry of the host galaxy, contribute to create a strong variation in the contribution from the host component,

which appears to vary from one instrument to another.

Early epoch spectra (< 50 days), the most prominent emission lines correspond to broad He II and Hα, shown in Figure 8. These lines have an average FWHM of $\sim 14,000$ km s^{-1} and $\sim 10,000$ km s^{-1} respectively. The analysis and evolution of their profiles is further explored in Section 4.2.

Several narrow absorption lines, associated with the host galaxy, were identified. The region around Hα contains an emission line that can be associated with [N II] at λ 6583. We also observed narrow absorption lines corresponding to Ba II at $\lambda\lambda$ 6496, the Na I D doublet at $\lambda\lambda$ 5889, 5896, Mg I $\lambda\lambda$ 5167, 5173, 5184, Fe I $\lambda\lambda$ 5266, 5324 Ca II is detected at $\lambda\lambda$ 3934, 3968 and as strong NIR triplet absorption at $\lambda\lambda$ 8498, 8542, 8662 Å.

4. ANALYSIS

### 4.1. *SED and bolometric lightcurve*

Swift host subtracted $UVW1$, $UVM2$, $UVW2$ photometry and Palomar data were used to fit the object blackbody temperature and radius. We fit the fluxes derived from each band with spherical blackbody emission models using Markov Chain Monte Carlo (MCMC) simulations, based on the Python package emcee (Foreman-Mackey et al. 2013). The blackbody bolometric luminosity, along with the best fit for the temperature and the radius are shown in Figure 6. Because only g-band measurements were available for our first detection epoch, we assumed that the luminosity follows a blackbody emission with a temperature of 21,000 K (average for the first 2 weeks) and scaled the flux to match the g-band magnitude.

The bolometric luminosity at peak is $L_p \simeq (1.0 \pm 0.15) \times 10^{43}$ erg s^{-1}. This is one order of magnitude lower than most of the optical TDEs (PS1-10jh, ASASSN-14ae, ASASSN-14li and ASASSN-15oi; see Figure 6). If compared to ASASSN-15lh, a TDE candidate from a rotating high-mass SMBH (Leloudas et al. 2016) [2], the peak is two order of magnitude fainter. Based on our M_{BH} estimate, we derive its Eddington luminosity $L_{\rm Edd} = 2.7^{+3.7}_{-1.6} \times 10^{44}$ erg s^{-1}, implying that at peak, iPTF16fnl shines only $2-10\%$ of $L_{\rm Edd}$. Assuming a radiative efficiency of $\eta = 0.1$, this translates into a peak accretion rate of $\dot{M}_{\rm peak} \sim 1.8 \times 10^{-3}$ M$_\odot$ yr^{-1} ($L = \eta \dot{M} c^2$).

Integrating the available bolometric luminosity (see Figure 6), we find the radiated energy to be $E_R = (2.0 \pm 0.5) \times 10^{49}$ erg. The accreted mass for this interval is $M_{acc} \sim 7.3 \times 10^{-5}$ M$_\odot$.

The rest-frame blackbody bolometric luminosity (Fig-

---

[2] This object is somehow controversial and has been initially interpreted as a superluminous supernova (Dong et al. 2016)
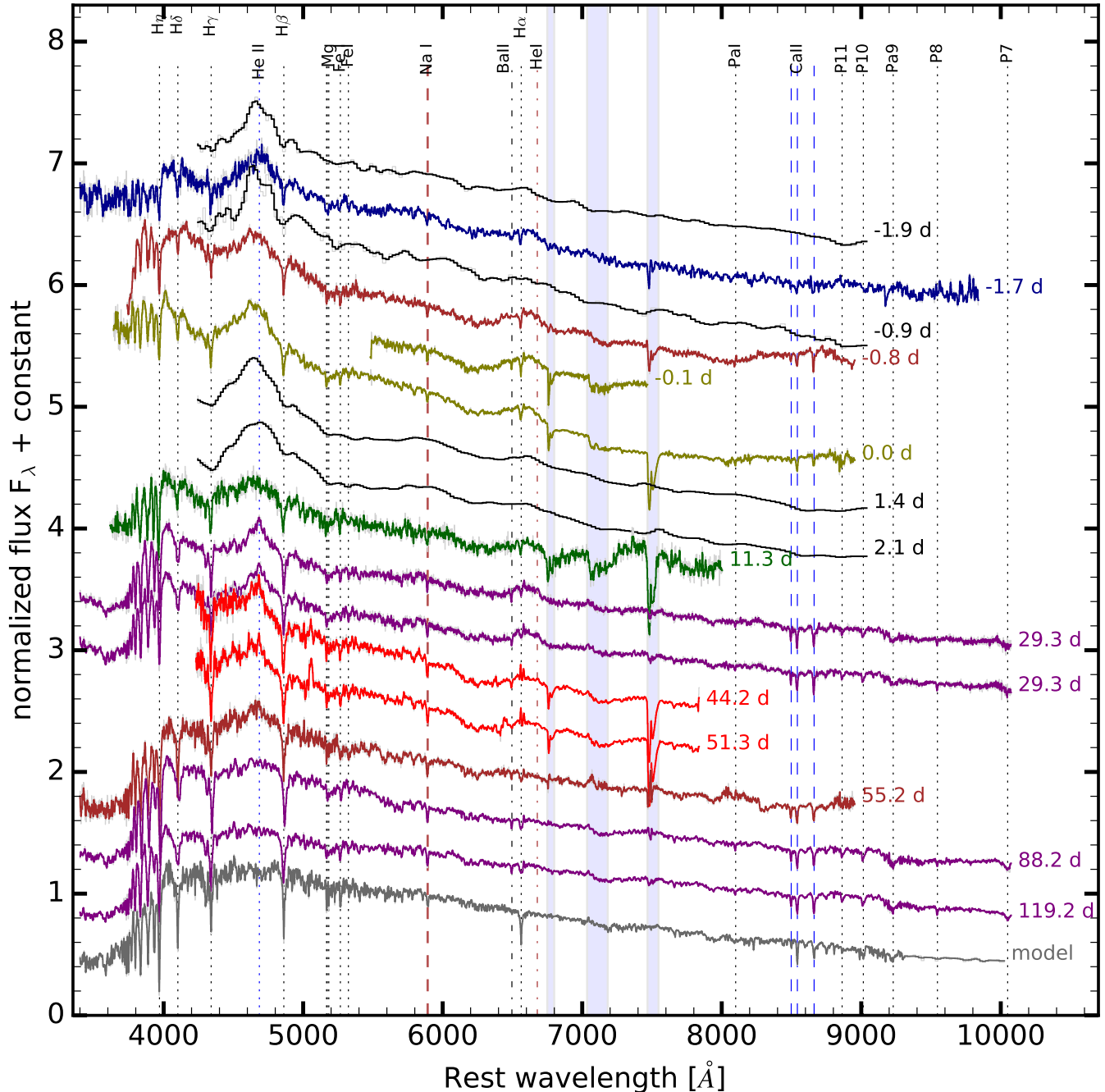
Figure 5. Spectral sequence of iPTF16fnl. The spectra are color coded by instrument: SEDM/P60 - black, DBSP/P200 - brown, 2 m LOYDS/LCO - blue, LRIS/Keck - purple, Deveny/DCT - green, GMOS-N/Gemini North - red and GTC/OSIRIS-olive. Telluric bands are marked with blue shaded areas. The labels on the top of the panel correspond to the main identified lines both from the TDE and the host galaxy. The spectra have been binned using the average of 3 pixels and low S/N areas were excluded from the plot. The best-fit galaxy model is shown in the bottom with gray colour.

ure 6) is fit with the characteristic power law $L \propto ((t - t_0)/\tau)^{-5/3}$ and an empirically motivated exponential profile, $L \propto e^{-(t-t_0)/\tau}$, where t_0 and τ are free parameters. For the decaying part of the lightcurve, the exponential model fits the data better ($\chi^2 = 17$ vs. 110), and best fit parameters are $\tau_0 \simeq 15$ and $t_0 \simeq -6$. For comparison, the decay for other optical TDEs is slower:

ASASSN-14ae had $\tau = 30$ days, whereas ASASSN-15oi and ASASSN-14li faded on timescales of 46.5 and 60 days respectively. Continued, high quality photometric monitoring would be required to draw conclusive results on long-term evolution, beyond the initial fading stage.

We estimate a lower limit for the time from disruption to peak light $t_{\text{peak}} \geq 11$ days from the bolometric

lightcurve. We select the measurements at ± 10 day from the peak in g-band and fit the luminosity with a 2 degree polynomial. For the raising part of the lightcurve, we use our only available g-band measurement. While this approach is widely used in estimating the explosion time for supernovae, the emission mechanism for TDEs is different and therefore it only yields to lower limits, as seen when applied to PS1-10jh.

Assuming that our bolometric lightcurve traces the rate of mass falling into the black hole, $\dot{M}(t)$, we use the lightcurve models from Guillochon & Ramirez-Ruiz (2013) (hereafter GR13), scaling them to the peak accretion mass rate and time to peak. The lightcurves are defined for a range of impact parameters $0.5 \leq \beta \leq 2.5$, where β is defined as the depth of the encounter $\beta = R_T/R_p$, R_T is the tidal disruption radius and R_p the pericentre radius. We impose a $M_{BH} = 2 \times 10^6$ $M_\odot$, but we leave the mass and radius of the disrupted star as free parameters. Our best fit corresponds to a star with polytropic index $\gamma = 4/3$ (fully radiative) with $M_* \sim 0.03\,M_\odot$, $R_* \sim 0.3\,R_\odot$ and a depth of the encounter comparable to the disruption radius ($\beta \simeq 1$). The lightcurve for the best fit model is shown in Figure 6. We obtain $t_{peak} \sim 11$ days, comparable with our previous naive estimate. If we impose that low mass stars are fully convective and fit for an object with $\gamma = 5/3$, we find a relatively good fit for a partial disruption ($\beta \sim 0.6$) and a similar value of $M_* \sim 0.06\,M_\odot$, although in this case t_{peak} is shorter than our observations suggest. Although these values illustrate that the disrupted object was likely a low-mass star, detailed modeling of the event would be required to draw quantitative results.

The blackbody model has an average temperature of $T_{BB} = 19,000 \pm 2000\,K$, which does not vary significantly over time, as shown Figure 6. At later epochs, the increased uncertainties in the host subtraction lead to increased scatter in T_{BB}. Given the uncertainty of the extinction in the host, these values can be assumed as lower limits. The model blackbody radius, R_{BB} starts at $\sim 2.5 \times 10^{14}$ cm, linearly declines for the first twenty days and then flattens to 5×10^{13} cm. These radii are much larger than the Schwarzschild radius $r_{Sch} \sim 6 \times 10^{11}$ cm of the nuclear black hole. In comparison, we note that the tidal disruption radius of such SMBH for a main sequence Solar-like star is $R_T \simeq 1 \times 10^{13}$ cm. Photospheric emission at radii larger than R_T is commonly observed for the optical sample of TDEs. This has been attributed to the existence of a reprocessing layer at larger radii, which re-emits the X-ray and UV in optical bands (Loeb & Ulmer 1997; Guillochon et al. 2014). Alternatively, the emission mechanism may originate from the energy liberated by shocks between streams in the apocenter, during the formation of the accretion disk

(Piran et al. 2015). Such an optically thick layer, mainly formed of stellar debris, is associated with the origin of the emission line signature for optical TDEs (Roth et al. 2016; Metzger & Stone 2016).
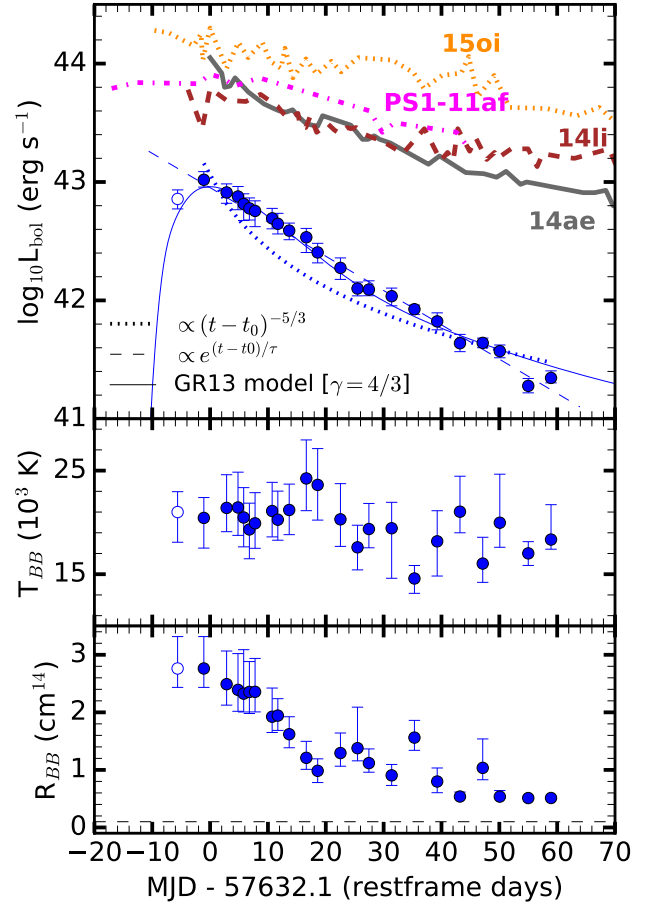
Figure 6. Top: Bolometric blackbody lightcurve for iPTF16fnl. Blue circles represent the fits with Galactic extinction correction only. The first (empty) data point was computed assuming an average blackbody temperature of 21,000 K (average for the first 2 weeks) and scaling the flux to match the g-band magnitude. The dashed line shows the best fit to a power law of the form $L \propto e^{-(t-t_0)/\tau}$. The dotted line shows the best fit to a $L \propto (t-t_0)^{-5/3}$. A solid line shows the best fit to GR13 models. Thick lines represent a sample of fast-fading TDEs for comparison: PS1–11af: dot-dashed magenta (Chornock et al. 2014), ASASSN-14ae: solid gray (Holoien et al. 2014), ASASSN-14li: dashed brown (Holoien et al. 2016b) and ASASSN-15oi: dotted orange (Holoien et al. 2016a). The reference MJD for the objects is the discovery date or epoch of peak luminosity (whenever available). Middle: Temperature evolution. Bottom: Evolution of the blackbody radius. (A color version of this figure is available in the online journal.)

4.2. *Spectroscopic analysis*

The early time spectrum of iPTF16fnl is dominated by blue continuum radiation and the characteristic broad
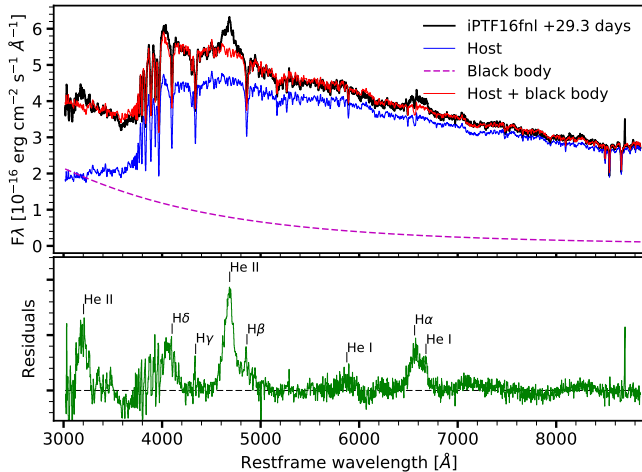
Figure 7. Example of host subtraction. The original spectrum, taken a +29.3 days (black thick line) was fit with a combination of host spectrum (blue solid line) and a blackbody fit (magenta dashed line). The best fit is shown with a red line. The residuals (corrected with a 2 degree polynomial) are shown in the lower panel. We mark the relevant emission lines. He II lines are clearly identified at $\lambda\lambda$ 3203 and 4686. He I lines are present at $\lambda\lambda$ 5875 and 6678. (A color version of this figure is available in the online journal.)

Table 3. Flux values for Hα and He II 4868Åfor the lines shown in Figure 8. The values were derived from the best model fit line profile. From the fit uncertainties, we estimate errors of 40% and 30% of the total flux for Hα and He II lines respectively.

MJD	Phase	Hα	He II
(d)	(d)	(erg s^{-1})	(erg s^{-1})
57630.4	−1.7	2.1×10^{40}	8.9×10^{40}
57631.0	−0.8	3.8×10^{39}	1.5×10^{40}
57631.3	0.0	6.6×10^{39}	8.3×10^{39}
57661.4	29.3	3.0×10^{39}	3.0×10^{39}
57661.4	29.3	2.1×10^{39}	2.5×10^{39}
57687.3	55.2	–	1.1×10^{40}
57694.4	62.3	–	2.7×10^{39}
57720.3	88.2	–	1.1×10^{39}

He II λ4686 line. The emission around 6500 Å can be attributed to Hα, although the He I λ6678 line is also detected. In the region around He II, we also detect Hβ in emission. However the strong host contribution makes its identification challenging at late times. In our analysis, we use the late time host spectrum (+119.2 days) as our template. We select the highest signal-to-noise (S/N) spectra, and fit them with a combination of host and a blackbody continuum, as show in Figure 7. On the residual spectrum, we fit a line model using the `python` package `lmfit` (Non-Linear Least-Squares Minimization and Curve-Fitting for Python). After masking the regions affected by telluric absorption, He II + Hβ and Hα + He I lines are fit using two component Lorentzian model, in order to derive the width (FWHM) and central location of the emission. The results, plotted as insets, are shown in Figure 8. The fluxes for each line are derived from the best fit model and shown in Table 3. As discussed in Brown et al. (2017), if all the flux in the He II line would be attributed to recombination produced by black body photoionizing radiation, the observed flux of $> 10^{40}$ erg s^{-1} would require black body radiation with temperature $\sim 4 \times 10^4$ K, which is higher than our fit, requiring an additional energy source to power this line.

Around peak, the He II lines appear to have higher velocity, showing an average value of FWHM$_{HeII} \simeq 14,000 \pm 3,000$ km s^{-1}, in contrast to the Hα line, with FWHM$_{H\alpha} \simeq 10,000 \pm 500$ km s$^{-1}$. At +30 and +45 days after peak, the FWHM narrows down to $8,500 \pm 1500$ km s^{-1} for He II and $6,000 \pm 600$ km s^{-1} for Hα. The center of the lines appears constant within the scatter for the first 90 days: for He II, the lines appear marginally blueshifted with velocity of -700 ± 700 km s^{-1}, while the Hα lines appear to be consistent with the reference wavelength, with a shift in velocity of -800 ± 1200 km s^{-1}.

5. DISCUSSION

iPTF16fnl is the faintest and fastest event in the current sample of optically discovered TDEs. Assuming our extinction estimation method is accurate, its luminosity at peak is one order of magnitude lower than any other optical/UV TDE discovered so far. Its timescale, as shown in Figure 10, also makes it as an outlier among the existing sample.

The host of iPTF16fnl is another example of a TDE in a post-starburst galaxy, further linking the propensity of TDEs to such galaxies (Arcavi et al. 2014; French et al. 2016). Moreover, E+A galaxy hosts seem to be exclusive for the lowest redshift TDEs ($z < 0.05$) (see Figure 10). The origin of the burst could be associated with a merger episode, as discussed in the case of ASASSN-14li (Prieto et al. 2016). The violent relaxation in the stellar orbits could enhance the rate of captures, as stars can undergo encounters that will scatter them towards the SMBH.

Lower SMBH masses ($< 10^7 M_\odot$) can increase the number of deeper encounters (Kochanek 2016), allowing for disruptions with smaller pericenter radius, R_p. However, theoretical works (Guillochon & Ramirez-Ruiz 2013; Stone et al. 2013) only show a weak correlation between the impact parameter β, and the peak of the flare. Therefore, the low luminosity and fast timescales shall be attributed to a lower mass black hole and/or lower mass for the disrupted star. Using our fit to TDE lightcurves from Guillochon & Ramirez-Ruiz (2013) with our estimated $M_{BH} \sim 2 \times 10^6 M_\odot$, we ob-
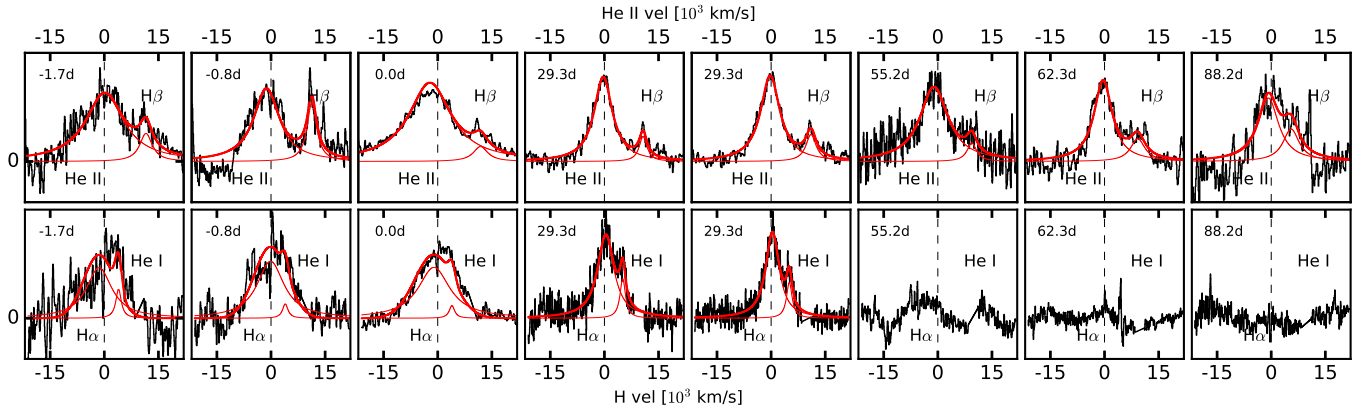
Figure 8. Residual normalized spectrum showing the line region around He II $\lambda4686$ (top row) and Hα (bottom row) lines for the higher S/N spectra of iPTF16fnl. In addition, the location of Hβ (top) and He I (bottom) lines are shown. Telluric regions, shown with shaded areas, were excluded from the fit. The first three epochs of Hα were fit using a Gaussian model, as the Lorentzian provided a worse fit. All the other lines were fit using a linear background and a Lorentzian line profile. We could not find a good fit for the last three epochs of Hα, but the spectrum is included for completeness. (A color version of this figure is available in the online journal.)
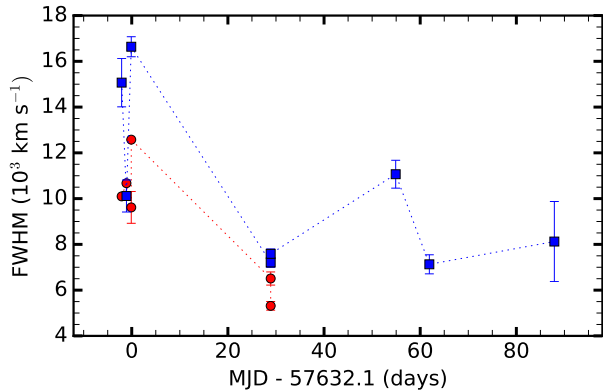
Figure 9. Top: Evolution of FWHM for He II $\lambda\lambda4686$ Å line (blue squares) and Hα (red circles) vs. phase of the spectrum. The last three epochs of Hα do not have a reliable measurement, and therefore are excluded form the figure. (A color version of this figure is available in the online journal.)

tain the mass of the disrupted star to be $M_* \sim 0.03$ for t_{peak} value of 11 days.

iPTF16fnl has clearly faster decay timescales than other TDEs, but also lower M_{BH}. Figure 11 shows a comparison of the e-folding timescale for iPTF16fnl and other optical TDEs, computed from exponential decay models, and the galaxy M_{BH}. There seems to be a trend between these two values for the optical/UV TDE population, in general agreement with the theoretical scaling between fallback timescale and black hole mass, $t \propto M_{BH}^{1/2}$. As a cautionary note, while literature generally reports M_{BH} based on bulge mass/luminosity, our best measurement is based on the $M - \sigma$ relation, although the bulge luminosity method yielded to similar results. Figure 10 shows that the most luminous flares ($L_{\rm bol} > 10^{44}$ erg s^{-1}) tend to fade on intermedi-

ate timescales, $\sim$50 days. However, there does not seem to be an evident correlation between the peak luminosity and the black hole mass, as discussed in Hung et al. (2017) (see their figure 15).

The tension between theoretical prediction of TDE rates and the ones inferred from observations is an active field of research. While it is difficult to explain the differences in terms of host galaxy properties (Stone & Metzger 2016), an observational bias towards the brighter events seems to offer a more plausible explanation. The discovery of iPTF16fnl has consequences for previous optical searches for nuclear tidal disruptions. In fact, its peak absolute magnitude $M_g = -17.2$ mag, and fast decay timescales, may mimic the behavior of a SN exploding close to the galaxy nucleus. Therefore, such faint events may have gone unnoticed in searches for bright ($M_g \sim -20$ mag) nuclear flares (Arcavi et al. 2014).

Systematic searches using the colour (including UV) and location of the transient, rather than its absolute magnitude, will increase our sensitivity to fainter flares. Consistent candidate selection using future surveys such as ZTF or LSST will allow us to explore the full luminosity function of tidal disruption flares. Spectroscopic confirmation of the candidates will be essential to identify this faint population. Dedicated instruments for transient classification such as SEDM will become the big players in this new era.
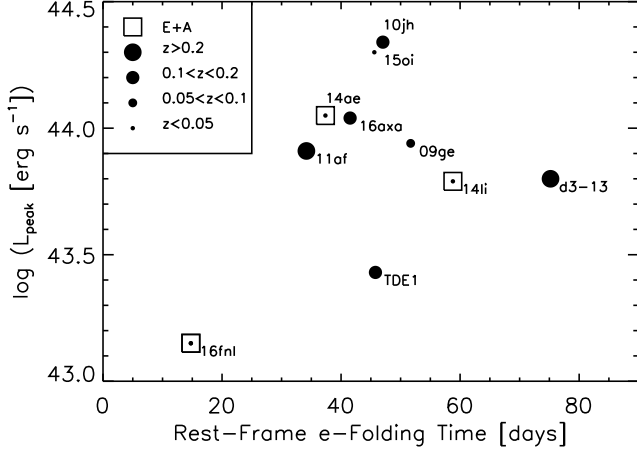
Figure 10. Comparison of the peak luminosity and decay time of iPTF16fnl with a sample of optical TDE from literature. The dot size encodes the redshift of the host galaxy. An external circle symbolizes the classification of the host galaxy as a post-starburst E+A galaxy. The optical TDE sample is based on published data: Gezari et al. (2008); van Velzen et al. (2011); Gezari et al. (2012); Chornock et al. (2014); Arcavi et al. (2014); Holoien et al. (2016b, 2014, 2016a) and Hung et al. (2017).
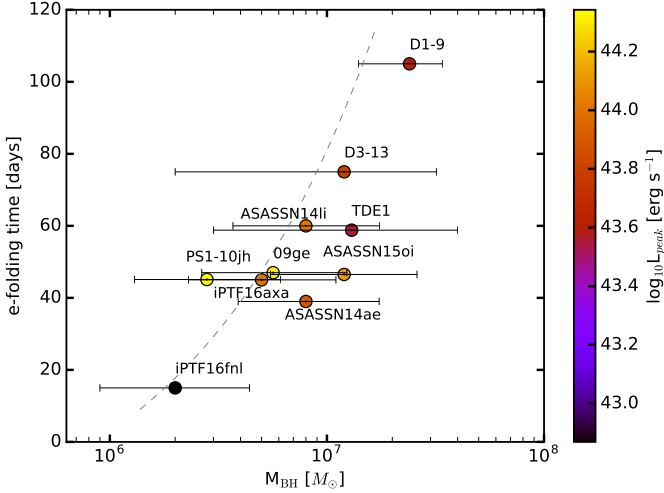
Figure 11. Mass of the host galaxy SMBH compared to the e-folding timescale for a sample of optical TDE. The dot color encodes the TDE peak luminosity. The peak luminosities were derived from literature: D1-9, D3-13 Gezari et al. (2008, 2009), PS1 (Gezari et al. 2012), PS1-11af (Chornock et al. 2014), ASASSN-14ae, ASASSN-14li, ASASSN-15oi (Holoien et al. 2016b, 2014, 2016a). The bolometric luminosities for TDE1 van Velzen et al. (2011) and 09ge (Arcavi et al. 2014) were derived by scaling the reported blackbody temperature emission to match the reported M_g. We assumed the standard dispersion in the McConnell & Ma (2013) relation whenever uncertainties for M_{BH} were not reported. A tentative correlation $t \propto (M_{BH})^{1/2}$ is provided to guide the eye (Guillochon & Ramirez-Ruiz 2013). (A color version of this figure is available in the online journal.)

6. CONCLUSIONS

We have presented the discovery and follow-up data for iPTF16fnl, a TDE candidate discovered by the iPTF survey on 2016 August 29th. The real-time image-subtraction pipeline and rapid spectroscopic classification allowed us to initiate a timely follow-up campaign. The photometric and spectroscopic signatures of iPTF16fnl are consistent with the sample of previous optically selected TDEs. As observed in other TDEs, the object shows very strong emission in UV wavelengths, with a $T_{BB} \simeq 19,000$ K. The temperature does not show strong evolution and the decrease in luminosity is best explained as a decrease in the size of the radiating region. In agreement with previous work, the size of this region, defined by its photospheric radius, is also about an order of magnitude larger than R_T. The early times, the spectroscopic signature of iPTF16fnl is dominated by He II and hydrogen lines, although we also detect emission from He I. After two months after peak light, most of the lines have faded. The exception is He II, which can be identified with a relatively constant FWHM of $\sim$7,000 km s^{-1}.

iPTF16fnl is remarkable in three ways: it is the nearest well studied optical/UV TDE (66.6 Mpc), and it has one of the shortest exponential decay timescales (about 15 days) and one of the lowest peak luminosities, $L_p \simeq (1.0 \pm 0.15) \times 10^{43}$ erg s^{-1}. Also, its host galaxy has the lowest M_{BH} among the optical sample of TDEs. Although this could justify the fast decay, its low luminosity may be related to the disruption of a lower mass star, or even a partial disruption.

Our work demonstrates that TDEs cover a wide range of luminosities and timescales. Current and future surveys, such as ATLAS, PS-1, ZTF and LSST, will provide large numbers of events with exquisite temporal coverage. Multifrequency follow-up of the candidates will lead to a better understanding of the underlying emission mechanism, hopefully leading to a unified multifrequency emission model. Large samples obtained with well understood selection criteria will be key to the study of TDE demographics, providing a unique link between theoretical studies of SMBH astrophysics and observations.

REFERENCES

Alam, S., Albareti, F. D., Allende Prieto, C., et al. 2015, ApJS, 219, 12

Alexander, K. D., Berger, E., Guillochon, J., Zauderer, B. A., & Williams, P. K. G. 2016, ApJL, 819, L25

Arcavi, I., Gal-Yam, A., Sullivan, M., et al. 2014, ApJ, 793, 38

Auchettl, K., Guillochon, J., & Ramirez-Ruiz, E. 2016, ArXiv e-prints, arXiv:1611.02291

Bade, N., Komossa, S., & Dahlem, M. 1996, A&A, 309, L35

Bell, E. F., McIntosh, D. H., Katz, N., & Weinberg, M. D. 2003, ApJS, 149, 289

Bianchi, L., Herald, J., Efremova, B., et al. 2011, Ap&SS, 335, 161

Bloom, J. S., Giannios, D., Metzger, B. D., et al. 2011, Science, 333, 203

Breeveld, A. A., Curran, P. A., Hoversten, E. A., et al. 2010, MNRAS, 406, 1687

Brown, G. C., Levan, A. J., Stanway, E. R., et al. 2015, MNRAS, 452, 4297

Brown, J. S., Kochanek, C. S., Holoien, T. W.-S., et al. 2017, ArXiv e-prints, arXiv:1704.02321

Brown, T. M., Baliber, N., Bianco, F. B., et al. 2013, PASP, 125, 1031

Bruzual, G., & Charlot, S. 2003, MNRAS, 344, 1000

Burrows, D. N., Hill, J. E., Nousek, J. A., et al. 2005, SSRv, 120, 165

Burrows, D. N., Kennea, J. A., Ghisellini, G., et al. 2011, Nature, 476, 421

Cabanela, J. E., & Aldering, G. 1998, AJ, 116, 1094

Calzetti, D., Armus, L., Bohlin, R. C., et al. 2000, ApJ, 533, 682

Cao, Y., Nugent, P. E., & Kasliwal, M. M. 2016, PASP, 128, 114502

Cappellari, M. 2016, ArXiv e-prints, arXiv:1607.08538

Cenko, S. B., Krimm, H. A., Horesh, A., et al. 2012, ApJ, 753, 77

Chabrier, G. 2003, PASP, 115, 763

Chornock, R., Berger, E., Gezari, S., et al. 2014, ApJ, 780, 44

Condon, J. J., Cotton, W. D., Greisen, E. W., et al. 1998, AJ, 115, 1693

Dong, S., Shappee, B. J., Prieto, J. L., et al. 2016, Science, 351, 257

Drake, A. J., Djorgovski, S. G., Mahabal, A., et al. 2009, ApJ, 696, 870

Dressler, A., Smail, I., Poggianti, B. M., et al. 1999, ApJS, 122, 51

Evans, C. R., & Kochanek, C. S. 1989, ApJL, 346, L13

Evans, P. A., Beardmore, A. P., Page, K. L., et al. 2009, MNRAS, 397, 1177

Fitzpatrick, E. L. 1999, PASP, 111, 63

Fixsen, D. J., Cheng, E. S., Gales, J. M., et al. 1996, ApJ, 473, 576

Foreman-Mackey, D., Hogg, D. W., Lang, D., & Goodman, J. 2013, PASP, 125, 306

Fremling, C., Sollerman, J., Taddia, F., et al. 2016, A&A, 593, A68

French, K. D., Arcavi, I., & Zabludoff, A. 2016, ApJL, 818, L21

Gehrels, N., Chincarini, G., Giommi, P., et al. 2004, ApJ, 611, 1005

Generozov, A., Mimica, P., Metzger, B. D., et al. 2017, MNRAS, 464, 2481

Gezari, S., Martin, D. C., Milliard, B., et al. 2006, ApJL, 653, L25

Gezari, S., Basa, S., Martin, D. C., et al. 2008, ApJ, 676, 944

Gezari, S., Heckman, T., Cenko, S. B., et al. 2009, ApJ, 698, 1367

Gezari, S., Chornock, R., Rest, A., et al. 2012, Nature, 485, 217

Gezari, S., Hung, T., Blagorodnova, N., et al. 2016, The Astronomer's Telegram, 9433

Guillochon, J., Manukian, H., & Ramirez-Ruiz, E. 2014, ApJ, 783, 23

Guillochon, J., & Ramirez-Ruiz, E. 2013, ApJ, 767, 25

Hills, J. G. 1975, Nature, 254, 295

Holoien, T. W.-S., Prieto, J. L., Bersier, D., et al. 2014, MNRAS, 445, 3263

Holoien, T. W.-S., Kochanek, C. S., Prieto, J. L., et al. 2016a, MNRAS, 463, 3813

—. 2016b, MNRAS, 455, 2918

Hung, T., Gezari, S., Blagorodnova, N., et al. 2017, ArXiv e-prints, arXiv:1703.01299

Jarrett, T. H., Chester, T., Cutri, R., et al. 2000, AJ, 119, 2498

Kochanek, C. S. 2016, MNRAS, 461, 371

Komossa, S. 2015, Journal of High Energy Astrophysics, 7, 148

Komossa, S., & Bade, N. 1999, A&A, 343, 775

Lacy, J. H., Townes, C. H., & Hollenbach, D. J. 1982, ApJ, 262, 120

Leloudas, G., Fraser, M., Stone, N. C., et al. 2016, Nature Astronomy, 1, 0002

Levan, A. J., Tanvir, N. R., Cenko, S. B., et al. 2011, Science, 333, 199

Loeb, A., & Ulmer, A. 1997, ApJ, 489, 573

Masci, F. J., Laher, R. R., Rebbapragada, U. D., et al. 2017, PASP, 129, 014002

McConnell, N. J., & Ma, C.-P. 2013, ApJ, 764, 184

Metzger, B. D., & Stone, N. C. 2016, MNRAS, 461, 948

Miller, A. A., Kasliwal, M. M., Cao, Y., et al. 2017, ArXiv e-prints, arXiv:1703.07449

Ofek, E. O., Laher, R., Surace, J., et al. 2012, PASP, 124, 854

Petrosian, A., McLean, B., Allen, R. J., & MacKenty, J. W. 2007, ApJS, 170, 33

Phinney, E. S. 1989, in IAU Symposium, Vol. 136, The Center of the Galaxy, ed. M. Morris, 543

Piran, T., Svirski, G., Krolik, J., Cheng, R. M., & Shiokawa, H. 2015, ApJ, 806, 164

Poole, T. S., Breeveld, A. A., Page, M. J., et al. 2008, MNRAS, 383, 627

Prieto, J. L., Krühler, T., Anderson, J. P., et al. 2016, ApJL, 830, L32

Rahmer, G., Smith, R., Velur, V., et al. 2008, in Proc. SPIE, Vol. 7014, Ground-based and Airborne Instrumentation for Astronomy II, 70144Y

Rees, M. J. 1988, Nature, 333, 523

Roming, P. W. A., Kennedy, T. E., Mason, K. O., et al. 2005, SSRv, 120, 95

Roth, N., Kasen, D., Guillochon, J., & Ramirez-Ruiz, E. 2016, ApJ, 827, 3

Sand, D. J., Brown, T., Haynes, R., & Dubberley, M. 2011, in Bulletin of the American Astronomical Society, Vol. 43, American Astronomical Society Meeting Abstracts #218, 132.03

Saxton, R. D., Read, A. M., Esquej, P., et al. 2012, A&A, 541, A106

Schlafly, E. F., & Finkbeiner, D. P. 2011, ApJ, 737, 103

Stone, N., Sari, R., & Loeb, A. 2013, MNRAS, 435, 1809

Stone, N. C., & Metzger, B. D. 2016, MNRAS, 455, 859

van Eerten, H., van der Horst, A., & MacFadyen, A. 2012, ApJ, 749, 44

van Velzen, S., Farrar, G. R., Gezari, S., et al. 2011, ApJ, 741, 73

van Velzen, S., Anderson, G. E., Stone, N. C., et al. 2016, Science, 351, 62

Vinkó, J., Yuan, F., Quimby, R. M., et al. 2015, ApJ, 798, 12

Voges, W., Aschenbach, B., Boller, T., et al. 1999, A&A, 349, 389

Willingale, R., Starling, R. L. C., Beardmore, A. P., Tanvir, N. R., & O'Brien, P. T. 2013, MNRAS, 431, 394

Table 1. Log of spectroscopic observations of iPTF16fnl.

MJD	Slit[a]	Telescope+Instrument	Grism/Grating	Dispersion	Resolution[b]	Exposure
(d)	(arcsec)			(Å/pix)	Å km/s	(s)
57630.2	3.0	P60+SEDM	none	25.5	540 (2900 km s^{-1})	900
57630.4	2.0	LCO 2-m+FLOYDS	–	1.7	15.3 (820 km s^{-1})	2700
57631.0	1.0	GTC+Osiris	1000B+2500I	2.12+1.36	7.1 (380 km s^{-1})	300
57631.0	1.0	GTC+Osiris	2500R	1.04	7.1(380 km s^{-1})	300
57631.2	2.2	P60+SEDM	none	25.5	504 (2700 km s^{-1})	900
57631.3	1.5	P200+DBSP	600/4000	1.5	10.5 (560 km s^{-1})	600
57633.5	3.6	P60+SEDM	lenslet arr.	25.5	672 (3600 km s^{-1})	1800
57634.2	3.0	P60+SEDM	lenslet arr.	25.5	613 (3300 km s^{-1})	1200
57636.2	3.0	P60+SEDM	lenslet arr.	25.5	659 (3500 km s^{-1})	1200
57637.2	3.6	P60+SEDM	lenslet arr.	25.5	589 (3200 km s^{-1})	1200
57638.2	3.0	P60+SEDM	lenslet arr.	25.5	556 (3000 km s^{-1})	1200
57643.22	1.0	VLT Kueyen+UVES	437+860	0.030+0.050	0.15 (8 km s^{-1})	2x1500
57643.25	1.0	VLT Kueyen+UVES	346+580	0.024+0.034	0.15 (8 km s^{-1})	2x1500
57643.4	1.5	DCT+Deveny	300	2.17	6.9 (370 km s^{-1})	600
57661.4	1.0	Keck I+LRIS	400/3400+400/8500	2.0	6.5 (350 km s^{-1})	600
57661.4	1.0	Keck I+LRIS	400/3400+400/8500	2.0	6.5 (350 km s^{-1})	600
57676.3	1.0	GeminiN+GMOS	–	1.35	8.1 (435 km s^{-1})	600
57683.4	1.0	GeminiN+GMOS	–	1.35	8.1 (435 km s^{-1})	1200
57687.3	1.5	P200+DBSP	600/4000	1.5	10.5 (560 km s^{-1})	600
57694.4	1.0	Keck I+LRIS	400/3400+400/8500	2.0	7.2 (390 km s^{-1})	1350
57720.3	1.0	Keck I+LRIS	400/3400+400/8500	2.0	6.5 (350 km s^{-1})	1800
57751.3	1.0	Keck I+LRIS	400/3400+400/8500	2.0	6.5 (350 km s^{-1})	1800

[a] For the IFU, the extraction radius (in arcsec) is indicated.
[a] Measured using the FWHM of λ 5577 O I sky line.

Wright, E. L., Eisenhardt, P. R. M., Mainzer, A. K., et al. 2010,
AJ, 140, 1868

Wyrzykowski, Ł., Zieliński, M., Kostrzewa-Rutkowska, Z., et al.
2017, MNRAS, 465, L114

Yaron, O., & Gal-Yam, A. 2012, PASP, 124, 668

Zabludoff, A. I., Zaritsky, D., Lin, H., et al. 1996, ApJ, 466, 104

Zauderer, B. A., Berger, E., Soderberg, A. M., et al. 2011,
Nature, 476, 425

Facility: DCT, Gemini North, GTC, Hale, JMCT, Keck:I, Keck:II, LCOGT, PO:1.2 m, PO:1.5 m, PS1, VLT

Software: AstroPy, EMCEE (Foreman-Mackey et al. 2013), IRAF, LMFIT, pPXF (Cappellari 2016), PTFIDE (Masci et al. 2017), PYRAF, UVOTSOURCE.

ACKNOWLEDGMENTS

APPENDIX

Table 2. Optical and UV photometry of iPTF16fnl in AB magnitude system.
These are the originally measured magnitudes with *Swift* and difference imaging piplines. For P48+CFH12k, the r-band column contains measurements in Mould-R filter system.
These measurements are not corrected for Galactic extinction. Table 2 is published in its entirety in the machine-readable format. A portion is shown here for guidance regarding its form and content.

MJD (days)	Telescope + Instrument	$UVW1$ (mag)	$UVM2$ (mag)	$UVW2$ (mag)	U (mag)	B (mag)	V (mag)	u (mag)	g (mag)	r (mag)	i (mag)
57626.4	P48+CFH12k	–	–	–	–	–	–	–	17.50±0.07	–	–
57629.4	P48+CFH12k	–	–	–	–	–	–	–	17.23±0.09	17.54±0.08	–
57630.8	Swift+UVOT	16.83±0.04	16.92±0.04	16.61±0.04	16.35±0.04	15.68±0.03	15.19±0.04	–	–	–	–
57631.7	P60+SEDM	–	–	–	–	–	–	17.13±0.09	17.17±0.07	17.42±0.12	–
...	...	...	...	...	...	...	...	...	...	...	...